High spatial resolution studies of epithermal neutron emission from the lunar poles: Constraints on hydrogen mobility

W. V. Boynton,[1] G. F. Droege,[1,2] I. G. Mitrofanov,[3] T. P. McClanahan,[4] A. B. Sanin,[3] M. L. Litvak,[3] M. Schaffner,[1] G. Chin,[4] L. G. Evans,[5] J. B. Garvin,[4] K. Harshman,[1] A. Malakhov,[3] G. Milikh,[6] R. Sagdeev,[6] and R. Starr[7]

Received 3 October 2011; revised 17 September 2012; accepted 18 September 2012; published 15 December 2012.

[1] The data from the collimated sensors of the LEND instrument are shown to be of exceptionally high quality. Counting uncertainties are about 0.3% relative and are shown to be the only significant source of random error, thus conclusions based on small differences in count rates are valid. By comparison with the topography of Shoemaker crater, the spatial resolution of the instrument is shown to be consistent with the design value of 5 km for the radius of the circle over which half the counts from the lunar surface would be determined. The observed epithermal-neutron suppression factor due to the hydrogen deposit in Shoemaker crater of 0.25 ± 0.04 cps is consistent with the collimated field-of-view rate of 1.7 cps estimated by Mitrofanov et al. (2010a). The statistical significance of the neutron suppressed regions (NSRs) relative to the larger surrounding polar region is demonstrated, and it is shown that they are not closely related to the permanently shadowed regions. There is a significant increase in H content in the polar regions independent of the H content of the NSRs. The non-NSR H content increases directly with latitude, and the rate of increase is virtually identical at both poles. There is little or no increase with latitude outside the polar region. Various mechanisms to explain this steep increase in the non-NSR polar H with latitude are investigated, and it is suggested that thermal volatilization is responsible for the increase because it is minimized at the low surface temperatures close to the poles.

Citation: Boynton, W. V., et al. (2012), High spatial resolution studies of epithermal neutron emission from the lunar poles: Constraints on hydrogen mobility, *J. Geophys. Res.*, *117*, E00H33, doi:10.1029/2011JE003979.

1. Introduction

[2] The possibility of volatiles, and particularly ice, being concentrated in permanently shadowed regions (PSRs) was suggested by *Watson et al.* [1961] and *Arnold* [1979]. The first evidence of this possibility was found by an analysis of radar reflection data from the Clementine mission [*Nozette et al.*, 1996], but others have raised questions concerning this result [*Stacey et al.*, 1997; *Simpson and Tyler*, 1999]. Data from the Lunar Prospector Neutron Spectrometer (LPNS) showed a significant reduction in the flux of epithermal neutrons in the vicinity of both lunar poles [*Feldman et al.*, 1998a], indicating an enhancement of hydrogen. *Elphic et al.* [2007] showed that the data were at least consistent with the enhanced hydrogen being in the PSRs, but the spatial resolution of the instrument was not sufficient to demonstrate such an association.

[3] More recently, the Lunar Exploration Neutron Detector (LEND) collected data with much better spatial resolution than that of LPNS [*Mitrofanov et al.*, 2010a]. The LEND instrument achieves its high spatial resolution using four ^{3}He detectors collimated with material that absorbs epithermal neutrons coming from more than a few degrees off axis. The instrument has a field of view (FOV) of 5.6° [*Mitrofanov et al.*, 2008, Figure 5], which translates to a 5-km radius of the circle over which half the counts would be determined at a 50-km altitude. On the other hand, an uncollimated instrument, such as LPNS or the uncollimated sensors on LEND, collects neutrons from horizon to horizon. With its higher spatial resolution, the LEND data showed that the small areas of depressed epithermal neutron flux, called neutron suppressed regions (NSRs), were not spatially consistent with the PSRs. In this work we shall show the processing that is used to generate maps

[1]Lunar and Planetary Laboratory, University of Arizona, Tucson, Arizona, USA.
[2]Deceased 17 August 2012.
[3]Institute for Space Research, RAS, Moscow, Russia.
[4]Astrochemistry Laboratory, NASA Goddard Space Flight Center, Greenbelt, Maryland, USA.
[5]Computer Sciences Corporation, Lanham, Maryland, USA.
[6]Department of Space Physics, University of Maryland, College Park, Maryland, USA.
[7]Department of Physics, Catholic University, Washington, D. C., USA.

Corresponding author: W. V. Boynton, Lunar and Planetary Laboratory, University of Arizona, Tucson, AZ 85721, USA. (wboynton@lpl.arizona.edu)

0148-0227/12/2011JE003979

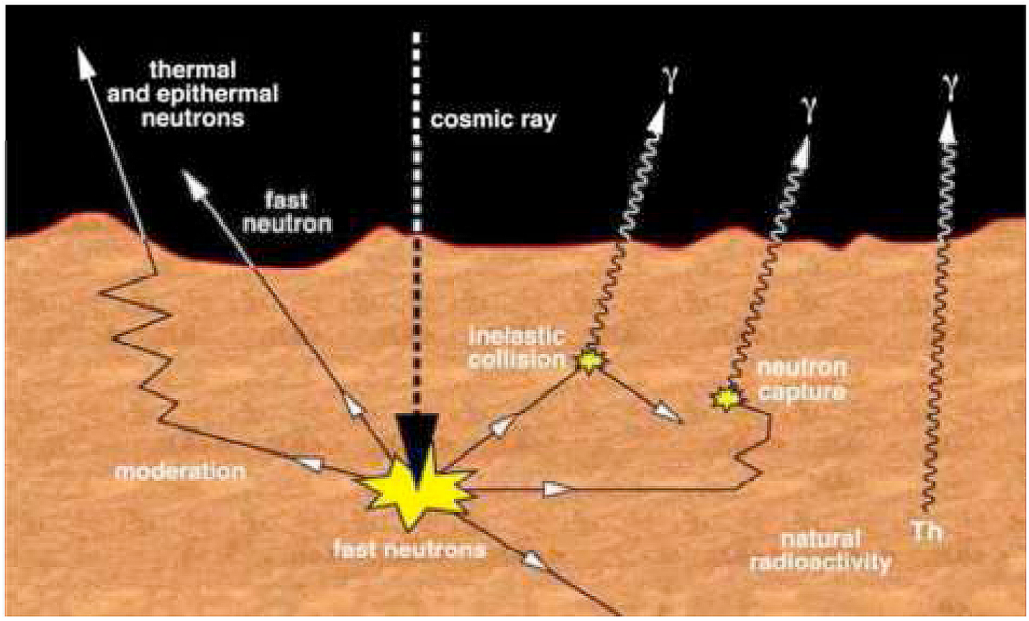

Figure 1. High-energy protons collide with nuclei in the soil to a depth of about 1 – 2 meters and produce secondary neutrons. The secondary neutrons are moderated by collisions with nuclei in the soil, and some of them escape the surface to be detected in orbit. Hydrogen nuclei are the most efficient at moderating neutron energy, and the escaping epithermal neutrons (those in the process of being moderated) provide a sensitive measure of the amount of hydrogen present.

and show how NSRs are determined. We shall also discuss some of the implications that the LEND results have for mobility of H via lunar processes.

1.1. Neutron Spectroscopy

[4] On planetary bodies with little or no atmosphere, bombardment by high-energy galactic cosmic rays and episodic solar energetic particles produces a cascade of secondary particles in the upper tens of centimeters of regolith. These cascades include secondary neutrons with energies of about 1–20 MeV, a portion of which may then escape and be measured in nearby space (Figure 1). Others are absorbed due to capture, or they decay due to their finite lifetime. The energy spectrum of emitted neutrons has a thermal component and a power-law tail from epithermal energies up to the original energy of the particles that were generated [*Drake et al.*, 1988]. The energy spectrum of the escaping neutrons depends on the composition of the soil and mostly on the content of hydrogen. Because H nuclei are the most efficient moderators of neutrons, even an amount as little as 100 ppm is known to produce a measurable change of epithermal neutron flux from the surface [*Mitrofanov et al.*, 2008]. Areas of enhanced hydrogen content in any of its chemical forms are found by looking for regions of lower-than-typical epithermal neutron counting rates.

[5] Related nuclear methods, specifically measuring gamma ray emissions, have been accomplished at the Moon (Luna-10) [*Vinogradov et al.*, 1966], (Apollo 15 and 16) [*Metzger et al.*, 1973], and (Lunar Prospector) [*Lawrence et al.*, 1998]; at Eros (NEAR Shoemaker) [*Evans et al.*, 2001]; and at Mars, (Mars Odyssey) [*Boynton et al.*, 2002, 2004]. Neutron spectrometers have flown aboard Lunar Prospector (LPNS) [*Feldman et al.*, 1998a, 2000; *Maurice et al.*, 2004; *Lawrence et al.*, 2006] and Mars Odyssey as part of the Gamma-Ray Spectrometer suite (The High Energy Neutron Detector, HEND) [*Mitrofanov et al.*, 2002; *Boynton et al.*, 2002] and

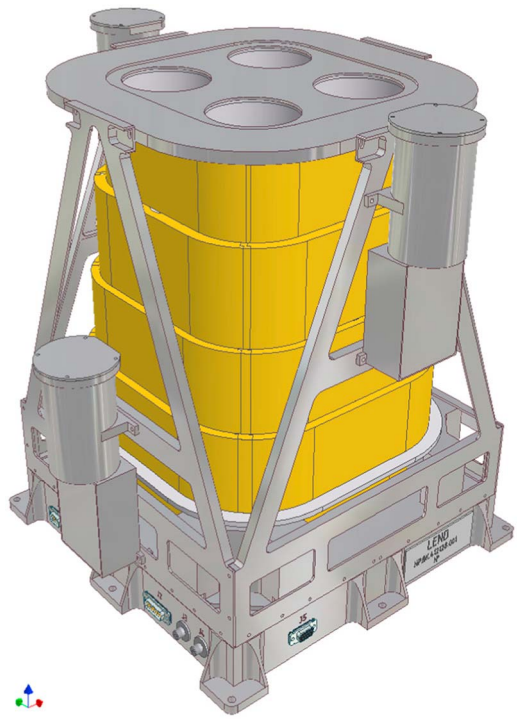

Figure 2. General view of the LEND engineering unit with the Module of Collimation MC.

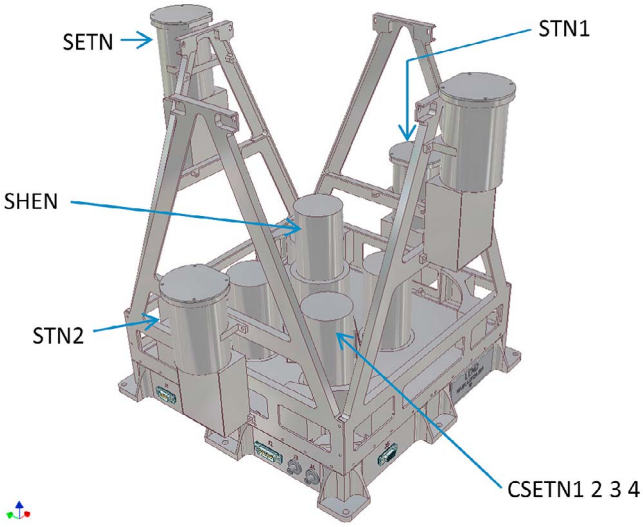

Figure 3. The nine sensors of LEND shown with the collimator module removed. The four sensors on the floor of the instrument are the Collimated Sensors for EpiThermal Neutrons, CSETN 1 to 4, which provide the data for this work.

The Neutron Spectrometer (NS) [*Feldman et al.*, 2004]). Neutron spectrometers have also recently arrived at Mercury on MESSENGER [*Goldsten et al.*, 2007] and at 4 Vesta (Dawn) [*Prettyman et al.*, 2003]. Another instrument, having a neutron detector with an active neutron source, DAN, has recently arrived at Mars (Mars Science Laboratory) [*Litvak et al.*, 2008; *Mitrofanov et al.*, 2012b].

1.2. LEND

[6] LEND, like HEND, is a Russian made and contributed instrument developed at the Institute for Space Research by the order of the Federal Space Agency of Russia in accordance with an implementation agreement between NASA and the Federal Space Agency. The LEND sensors and their electronics design are derived from HEND. The major distinction between LEND and HEND is the presence of a collimation module, which absorbs neutrons from outside a narrow FOV. Data processing and analysis procedures are in part modeled after Mars Odyssey Gamma Ray Spectrometer (GRS) [*Boynton et al.*, 2002] and HEND methods. Details of the LEND concept design and instrumentation are presented in *Mitrofanov et al.* [2008, 2010b].

[7] LEND consists of eight ^{3}He tubes and a scintillator to measure fluxes of thermal, epithermal, and fast neutrons (Figures 2 and 3). There are two separable modules: the Module of Sensors and Electronics (MSE) and the Module of Collimation (MC). The four Collimated Sensors of Epithermal Neutrons (CSETN1-4) are located inside the MC and are also enclosed by Cd shields to absorb thermal neutrons. These collimated sensors are the main innovated part of the instrument and provide the mapping capability of lunar epithermal neutrons with the horizontal spatial resolution about 5 km from a 50 km orbit.

[8] The ^{3}He nucleus has one fewer neutron than the main isotope of Helium (^{4}He or alpha particle), and it has a large cross section for capture of low energy neutrons in the reaction n + ^{3}He→^{3}H + p + 764 keV. The released energy of the reaction is distributed between a triton, ^{3}H, and a proton with 191 keV and 573 keV energies, respectively, in inverse proportion to their masses [*Knoll*, 2000]. The ^{3}He counter produces an electrical pulse proportional to the energy deposited in the detector volume. Pulse heights are binned into one of 16 logarithmically spaced channels, and counts in channels 10 to 16 are summed and used as the sensor counts for neutrons [*Litvak et al.*, 2012b]. Pulse-height spectra from each LEND detector are collected on 1-second intervals.

[9] The four ^{3}He collimated sensors, CSETN1-4, are installed inside the collimating module, which absorbs most of the external neutrons outside of the instrument FOV (Figure 4). One of the best absorbing materials is ^{10}B, and its absorption efficiency becomes much higher when neutrons are slower. External layers of polyethylene are used to moderate the energy of incident neutrons, and internal layers of ^{10}B then provide efficient absorption. The FOV of LEND

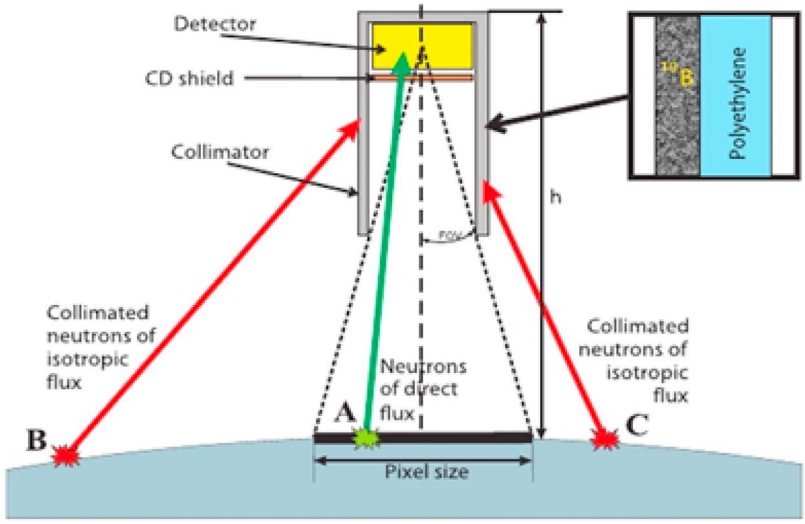

Figure 4. Schematic concept of neutron collimation. The layer of polyethylene moderates neutrons of higher energy to energies low enough that they can be absorbed by the layer of ^{10}B.

Table 1. Days in Which Data Are Excluded Due to Solar Particle Events (Determined From GOES and ACE Data)

Day of Year	Dates
2010 163–165	Jun 12–14
2010 215	Aug 3
2010 244–245	Sep 1–2
2011 28–29	Jan 28–29
2011 46–48	Feb 15–17
2011 67–72	Mar 8–13
2011 79–83	Mar 20–24
2011 94–95	Apr 4–15

for epithermal neutrons (5.6°) provides for the examination of neutron suppressed regions on a scale comparable to the largest PSRs.

1.3. LRO Mission

[10] The science phase of the mission began with the attainment of lunar polar orbits of 50 km altitude with variations from 30 to 70 km. The orbits have a period of approximately 2 hours separated by roughly 1.07° longitude providing LEND with complete mapping of the lunar surface every 14 days.

[11] LEND operates autonomously, collecting data throughout the lunar orbit and generating approximately 0.26 Gbits of measurement data per day. High voltage (~2 kV) to the detectors is turned off during biweekly station keeping maneuvers due to risk of corona discharge during propulsion events.

2. Reduction of LEND Collimated Sensor Data

[12] The LEND on board the Lunar Reconnaissance Orbiter (LRO) has continuously mapped the neutron flux from the Moon since July 2009. This section describes the step by step process used to reduce the raw collimated detector data into corrected higher level derived products. The data presented in this work are from 15 September, 2009 through 24 May, 2011.

2.1. Solar Energetic Particle Events

[13] Both the collimated and uncollimated sensors aboard LEND are sensitive to Solar Energetic Particle (SEP) events. We monitor proton fluxes from GOES-13 (http://swpc.noaa.gov/ftpmenu/warehouse.html) and ACE (http://www.srl.caltech.edu/ACE/ASC/DATA/level3/sis/Counts.cgi?LATEST=1) to remove LEND data associated with them. The onset of the SEP event is obvious with a very rapid change in particle flux; the end of the event is defined as when the SEP count rate returns to the pre-event rate. To be conservative, we exclude LEND data over the entire UTC day in which the onset and end occurs. All count rates are assigned a value of −1 for records that occur in an SEP interval. A table of SEP intervals based on GOES-13 and ACE data over the first 23 months of the mission is shown in Table 1.

2.2. Outlier or Off-Limit Events

[14] Infrequent, sporadic, and randomly distributed 'outlier' values are seen in the raw detector count rates when summing channels 10–16. These outliers could be produced either due to some micro-discharge in the HV circuit of a counter, or due to some corruptions in the instrument memory. The data with outliers is excluded from the mapping data together with their associated time intervals. Histograms were constructed for each detector's counts to ascertain a standard by which to call a particular record an 'outlier' event (Figure 5). Based on these results, we set the limit on outlier values to be any detector record where the

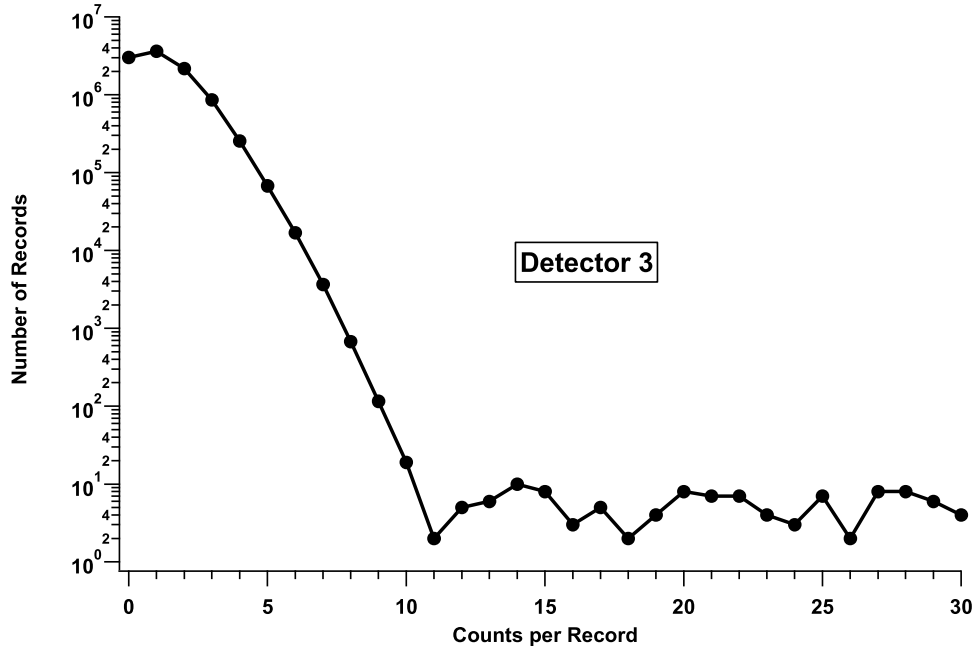

Figure 5. Histogram of total detector counts in channels 10 through 16. Records with counts >11 are considered outlier values. They constitute only 0.01% of recorded events.

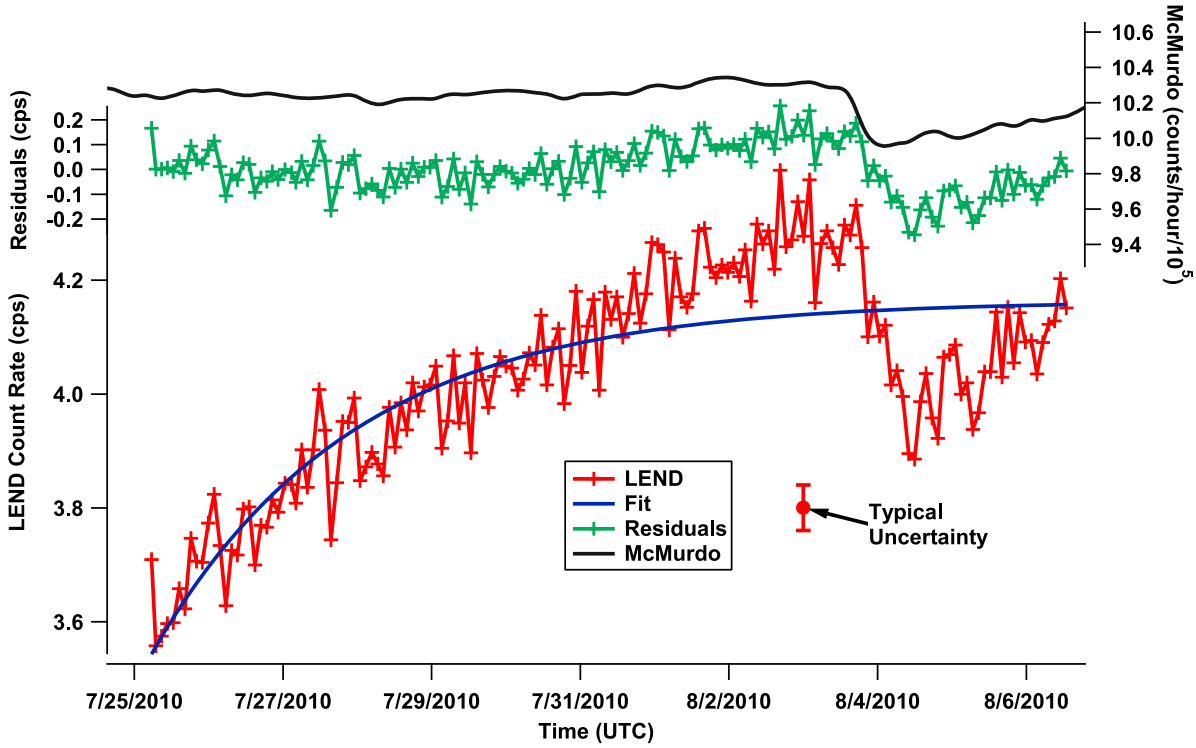

Figure 6. Typical warm-up cycle based on the orbital average count rate of all collimated sensors. Fitting parameters are determined separately on each detector to correct for slightly different warm-up curves in each detector, but the orbital average of the sum of count rates in all four detectors (shown here) is used to correct for the short-term cosmic-ray variations. Deviations from the fit are due to short-term changes in the cosmic-ray flux as can be seen in these data from the McMurdo Antarctica cosmic-ray monitoring station. Corrections for short-term variations in the cosmic-ray flux are made based on a 24-hour moving average of the residuals. The McMurdo data are also 24-hour smoothed, and they have been interpolated to the same times as the LEND orbital averages. A typical error bar is shown for the standard error of the orbital averages. The scatter in the data is often larger than the error bar would suggest due to short-term cosmic-ray flux variations.

sum of the counts in channels 10 through 16 is greater than 11. Typically, a count rates of 12 cps or higher represents at least a seven-sigma event relative to the mean of about 1.25 cps. Detector records that are defined as outlier events are not used, and they are also assigned count rate values of −1 when converting to a derived record.

2.3. Off-Nadir Measurements

[15] Occasionally, particular instruments on board LRO have requested off-nadir slews for targeted observations. The nadir angle–the angle between the LEND bore-sight and nadir vectors–is recorded for each raw record. If the nadir angle is greater than 1°, the record is ignored and a value of −1 is assigned to its count rate in the corresponding derived record.

2.4. Correction for Instrument Warm-Up

[16] The LEND ^{3}He sensors have a high sensitive volume and pressure of 20 atm. These sensors gradually increase in efficiency by 15–20% after each of the approximately biweekly turn-on cycles due to accumulation of charge on the insulators that support the center electrode wire. Before this charge build-up, there is a dead volume at each end of the tube, but the charge build-up on the insulator essentially increases the active length of the center electrode and thus decreases the dead volume. A typical efficiency warm-up cycle for a collimated sensor is shown in Figure 6 (see section 2.5).

[17] Valid on-intervals are those intervals that are at least 7 days long. Data from the first six hours after turn on are not included in the processing to allow for occasional rapid change in detector efficiency. Records falling outside these valid intervals are not included in the orbital averaging or conversion to derived records. In the first two years of data collection, there are ~65,700,000 raw records. A summary of records available and restricted based on this definition is given in Table 2. Outlier, off-nadir, and SEP interval records are not used in the orbital averaging or in generating derived records.

[18] Orbital average data are generated from all valid records taken pole-ward of 60° latitude to avoid variations due to maria at lower latitudes that shows an enhancement due to fast neutrons. Curves are generated for each detector (i) for each 'on' interval (j) and are fit to an exponential,

$$A_{i,j} * \left(1 - e^{-k_{i,j} * \left(t - t^0_{i,j}\right)}\right), \quad (1)$$

Table 2. LEND Record Statistics for the Period September 15, 2009 to May 24, 2011

Condition	Number of Records	Fraction
Total raw records	59,637,213	
All detectors off (station keeping) or not in valid interval (<7 days long)	9,829,514	16%
Off-nadir pointing	2,868,804	4.8%
SEP interval	1,209,60	2.0%
Records with an outlier event	7,671	0.01%
Records converted to derived records	45,729,295	

where t is the time, and $A_{i,j}$, $k_{i,j}$, and $t^0_{i,j}$ are fitting parameters (Figure 6). The fits are weighted by the reciprocal of the square of the standard error of the mean for each orbital average. The constant $A_{i,j}$, is the counting rate of the detector at efficiency saturation.

2.5. Correction for Cosmic-Ray Variation

[19] The solar cycle modulates the flux of galactic cosmic rays entering the solar system from elsewhere in the galaxy. As a consequence, the cosmic-ray flux in the inner solar system varies with time and is anti-correlated with the overall level of solar activity. Cosmic rays are the excitation source for lunar neutrons, so the LEND data must be normalized to their variation.

[20] The $A_{i,j}$ values showed little variation over the first six 'on' periods (around 3 months), indicating that there was little change in the cosmic-ray flux. These six values for each detector were averaged to generate long-term normalization values $A^0_1, A^0_2, A^0_3, A^0_4$ (Table 3). Subsequent $A_{i,j}$ values showed a gradual decrease over time due to the lower cosmic-ray flux as solar activity increased; all subsequent data were normalized by the ratio of the current $A_{i,j}$ to its A^0_i. The adjusted count rate for each detector is given by:

$$R^{adj}_i = C_i \, A^0_i \Big/ \left(1 - e^{-k_{i,j} * \left(t - t^0_{i,j}\right)}\right), \tag{2}$$

where C_i are the counts in detector i and the denominator adjusts for the change in detector efficiency due to warm-up. Because LEND counts over a 1-second accumulation time, the recorded counts are simply converted directly to a rate; the count rates are so low that no dead-time correction is needed.

[21] These A^0_i values are also used as a measure of efficiency differences between detectors when we have to adjust for a detector not providing data for a given record, either because it is intentionally turned off, or because it may have generated a count determined to be an outlier. For these cases we take the average adjusted count rate for the "on" detectors and assign that average rate to the "off" detectors with an adjustment for differences in efficiency based on their A^0_i ratios. This adjustment is given as:

$$R^{adj}_{off} = \frac{A^0_{off} * \sum R^{adj}_{on}}{\sum A^0_{on}} \tag{3}$$

For example, if the adjusted count rates of detectors 1 and 2 are 1.25 cps and 2.20 cps, respectively, and detectors 3 and 4 are off, we find that the adjusted rate for detector 3 is (1.2426 * 3.45)/2.3785 = 1.80 cps; similarly, the rate for detector 4 is 1.93 cps. The final adjusted count rate is simply the sum of the adjusted rate of all four detectors:

$$R^{adj}_{total} = \sum_{i=1}^{4} R^{adj}_i. \tag{4}$$

[22] At this point, the data have been adjusted for changes in efficiency and for long-term changes in the cosmic-ray flux, but one additional correction needs to be made for short-term (10s of hours) changes in the cosmic-ray flux. Changes in the flux of cosmic rays can be seen both in the cosmic-ray flux at Earth and in occasional anomalies in the orbital average data relative to the fit of the warm-up efficiency function. Figure 6 shows an example of this effect seen in the residual to the warm-up efficiency fit. The residual is compared to the terrestrial cosmic-ray flux as measured at McMurdo, Antarctica (http://neutronm.bartol.udel.edu/), where a similar effect is seen. We take the residual to the warm-up fits as a means to correct for short-term variations in the neutron flux. We are confident in this assignment because: (1) we see the same effects at the same time at both poles, (2) the effects are seen simultaneously in all four detectors, and (3) there is a significant correlation over the course of the mission between the McMurdo data and the residuals of the warm-up fits (significance > 99.9%).

[23] Because we see the same effect over all four detectors, we make another fit to the orbital averages, but this time it is on the combined count-rate data from all four detectors to improve statistics. We generate smooth curves as a 24-hour moving average of the residuals, and this curve is then used for a point by point correction of each collimated record. Essentially the 24-hour-smoothed GCR variations get distributed back into each of the individual detector records. The short-term cosmic-ray correction factor (CRCF) is evaluated at each raw record's collection time as

$$CRCF(t) = 1 - ResidualSmooth/A_{i,j} * \left(1 - e^{-k_{i,j} * \left(t - t^0_{i,j}\right)}\right) \tag{5}$$

For example, if the residual is 0.04 cps high and the value of the fit function is 4.00 cps, we multiply by

$$1 - (0.04/4) = 0.99 \tag{6}$$

We find that the CRCF shows a standard deviation of about 1%, and thus it is an important correction to make because we are looking for count rate differences on the

Table 3. Average Count Rates of Collimated Detectors at the Beginning of the Mission (cps)

	Count Rate
A^0_1	1.0939 ± 0.0040
A^0_2	1.2846 ± 0.0056
A^0_3	1.2426 ± 0.0067
A^0_4	1.3285 ± 0.0064

order of 0.01 cps or about 0.2%. The complete equation for the corrected count rate of each detector then becomes

$$R_i(t) = C_i\, A_i^0 \Big/ \left(1 - e^{-k_{i,j} * \left(t - t_{i,j}^0\right)}\right) * CRCF(t). \quad (7)$$

2.6. Uncertainties on Count Rates

[24] It is clear that the relative uncertainties on the corrected counts for any given record are significantly greater when one or more of the detectors is not producing valid data. In order to make maps, we need to calculate an average count rate of many records from a given location on the Moon. Thus we need to properly weight the data in calculating the average, *e.g.* a record in which four detectors return valid data must be given more weight than a record in which only two or three detectors' records are valid.

[25] We weight by the reciprocal of the variance, but estimating the variance with such a low number of counts is not straightforward. Normally one assumes the variance in the number of counts recorded is simply the number of counts. With a large number of counts, such an assumption is a reasonably good approximation to the true variance of the counts. It is important to remember, however, that the number of counts only yields our best estimate of the variance, s^2, which is not generally equal to the true variance, σ^2. For example, a record with 2 counts and one with 4 counts are both common occurrences, but the record with 2 counts would be given twice as much weight if the variance were simply taken as the number of counts. Such weighting gives a systematically low result.

[26] This distinction is particularly important with LEND data since the counts in these records are so small. With the low counting rates present in our records, we must have a better means for estimating the variance. We use the value of the exponential efficiency function described above. This function is typically fit over a few hundred thousand records in each power 'on' cycle and is thus a much better estimate of the true variance at the time the data were collected.

[27] Because we adjust the observed count rates to account for instrument warm-up and cosmic-ray variations, we also have to adjust the observed variance. The variance, $ó^2$, for each raw (uncorrected) detector record is thus

$$ó_{i,j}^2 = \left(A_i^0\right)^2 * CRCF^2 * \frac{A_{i,j}}{\left(1 - e^{-k_{i,j} * \left(t - t_{i,j}^0\right)}\right)}. \quad (8)$$

The variance on the total count rate of all four detectors is simply the sum of the variances of the individual detectors, but when one or more detectors fails to provide a valid count, then the variance on the total rate is the sum of the variances of the 'on' detectors multiplied by the square of the factor by which the 'on' rates were increased to give the total rate. In this case the variance on the total is given by

$$ó_R^2 = \sum_{on} ó_{i,j}^2 * \left(R \Big/ \sum_{off} R_i\right)^2 \quad (9)$$

Continuing with the example at equation (7), assuming the two $ó_{i,j}^2$ for the on detectors are identical at 1.20 cps^2. The sum of all four adjusted count rates, R, is 7.18 cps, and we then find that $ó_R^2 = 2.40 * (7.18/3.73)^2$, $= 8.89\ cps^2$, showing that the uncertainty of the result is about double that of having all four detectors returning valid data, in which case $ó_R^2 = 4.8\ cps^2$.

[28] In section 6 we provide a reduced chi squared test that shows that our treatment of uncertainties is appropriate.

3. Mapping the Data

[29] Because we are looking for changes in count rates on the order of 0.01 cps, which is 0.2% of the typical 5 cps counting rate for the sum of all four detectors after correction for cosmic-ray and detector-efficiency variations, we must combine approximately 50,000 1-second data records to obtain that statistical precision. We combine all of the records accumulated over the same location on the surface into equal area (3.0 km^2) HEALPix bins [*Gorski et al.* 2005]. We combine the data by making a weighted mean of the count-rate records in each bin. The weighting is by the reciprocal of the variance of each record assuming Poisson counting statistics. (See section 2.6 for a discussion of the need to weight the data and the method used to determine the variance.)

[30] This bin size is so small that in order to get reasonable counting statistics, we must smooth the data to average out the noise in the weighted-mean bins. We perform a weighted box smoothing with a radius given in degrees of arc by

$$1.64 * \left(0.2 + \sqrt{\cos(latitude)}\right) \quad (10)$$

The smoothing radius is made a function of latitude to allow for the fact that there are fewer orbits per degree of longitude with increasing distance from the pole. Without this change in smoothing radius, the signal-to-noise ratio would be significantly worse at lower latitudes. In calculating the average count rate in each smoothing box, we weight the values used in the smoothing by the reciprocal of the variance of the weighted-mean values. Figure 7 shows the smoothed count rate maps for both the North and the South. The statistical uncertainties on the smoothed count rates are given by the standard error of the values used in the smoothing box and are shown in Figure 8 for the South; the uncertainties in the North are similar. The uncertainties are not symmetric about the poles because the orbits have a small inclination, and the instrument is regularly turned off for short time periods—generally corresponding to 90° and 270° longitude—for spacecraft station-keeping maneuvers. The extent of smoothing is always a compromise between degrading spatial resolution and improving statistics. An example of this compromise is presented in section 6.

4. Background Correction

[31] In addition to the counts generated by epithermal neutrons in the field of view of the collimators, there are several background sources of counts. Calculations based on an analysis of flight data [*Mitrofanov et al.*, 2011] were used to calculate the extent of these background counts as follows. In addition to the desired signal in the collimator field of view, the sensors also detect high-energy lunar neutrons coming through the collimator walls (~0.3 cps), lunar

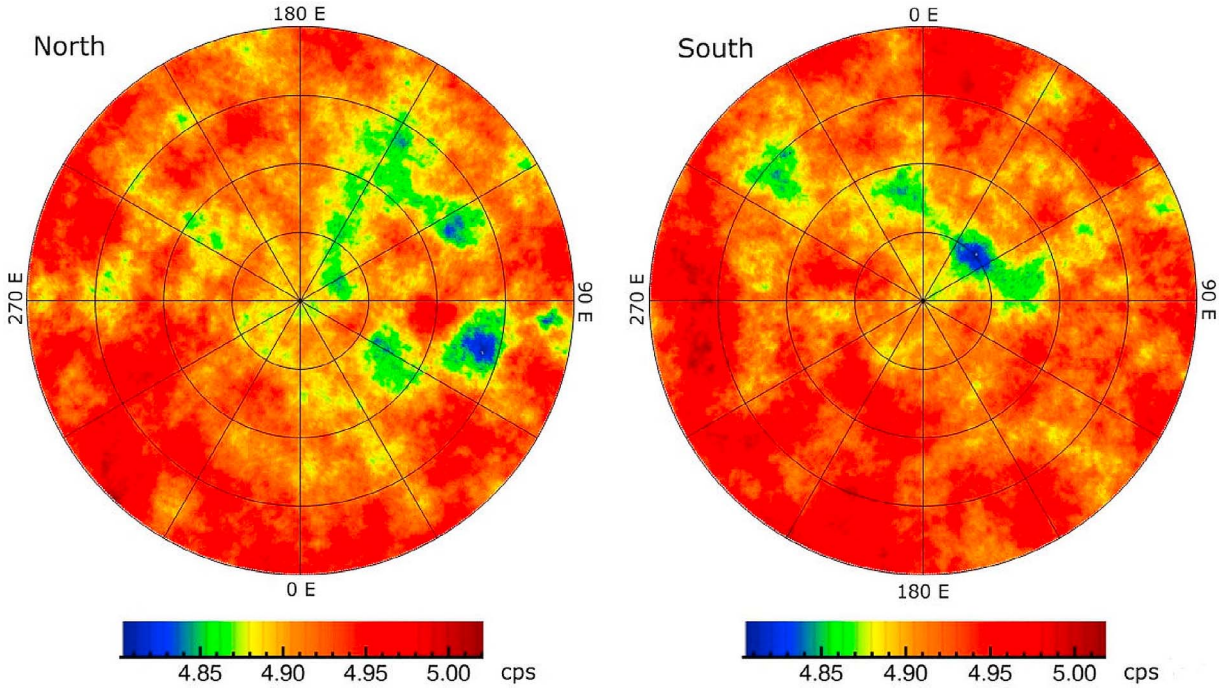

Figure 7. Smoothed count-rate maps of the North and South Polar regions to latitude 82° using the LEND collimated sensors. Significant flux depressions related to enhanced hydrogen are observed.

neutrons scattered off the spacecraft (~0.8 cps), and neutrons produced directly in the spacecraft due to cosmic-ray interactions (~2.2 cps). After subtraction of the background components from the observed count rate of about 5 cps, the net count rate due to epithermal neutrons in the collimator field of view is about 1.7 cps, but it can range from 1.5 to 1.9 cps with systematic uncertainties in the estimates of the various background contributions [*Mitrofanov et al.*, 2010a]. Although the absolute value of the background is uncertain by about 0.2 cps, its exact value is not so important in this work since we are concerned with the small-scale spatial differences in count rates rather than the absolute values.

[32] The 2.2 cps of background, due to direct cosmic-ray interactions with the spacecraft, is independent of lunar hydrogen distribution, because ~1.1 cps of the background is due to lunar neutrons, the background is not uniform. This part of the background is spatially dependent on the location of the spacecraft and the corresponding flux of lunar neutrons coming from the large area (limb to limb) that is outside the collimator field of view. We therefore have to calculate the background by accounting for the emission rate of neutrons from everywhere within view of the spacecraft. To be conservative, we make the assumption that the neutrons that pass through the walls of the collimator are related to the observed flux of epithermal neutrons at different locations within view of the spacecraft. Making this assumption is conservative with respect to spatial variation of the background both because most of the neutrons that pass through the walls of the collimator are high-energy neutrons, which do not show as much spatial variation over the polar regions as epithermal neutrons [*Feldman et al.*, 1998b], and the higher energy neutrons show less beaming

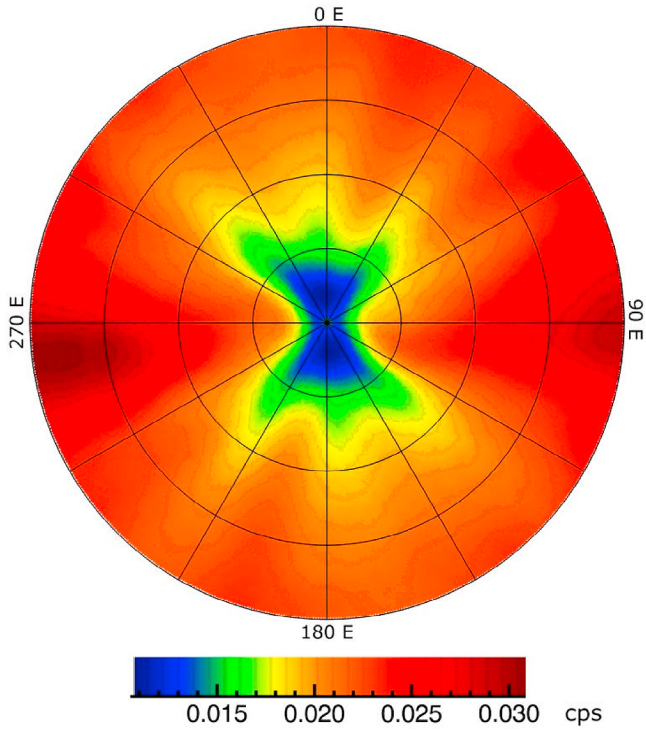

Figure 8. Statistical uncertainties in the LEND count rates at the South Pole; the North Pole uncertainties are nearly identical. The longitudinal dependence is due to the instrument being shut off at various times, most of which occur near 90° and 270°E longitude due to spacecraft rocket motor firing for momentum management.

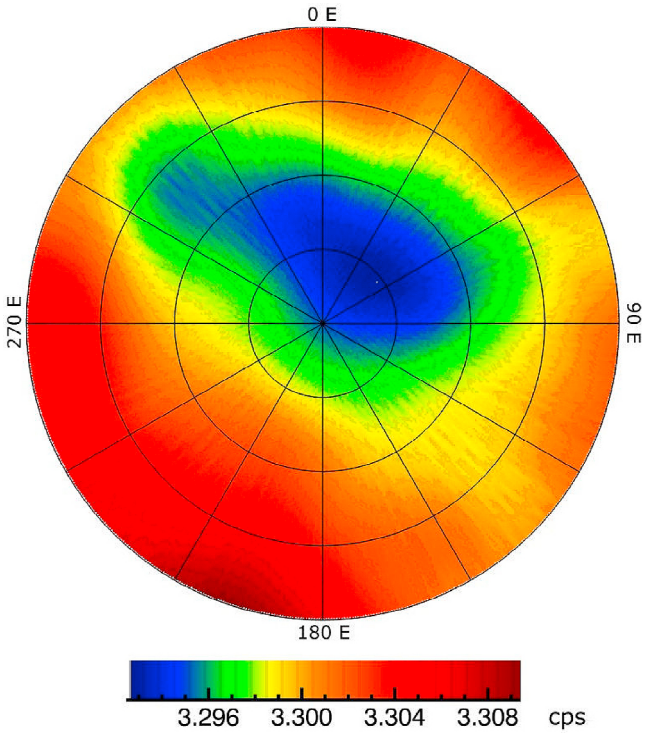

Figure 9. Map of background counts at the South Pole due both to lunar neutrons from outside the collimator field of view and cosmic-ray produced neutrons from the spacecraft. It is important to note that because the background is determined by neutrons coming from such a very large area (limb to limb) it does not change significantly over the small spatial scales of the NSRs. Because the background variation is negligible over small spatial scales, any observed fluctuations in count rate seen over tens of km are either due to statistical noise or true variations in hydrogen content.

toward the zenith than the low-energy epithermal neutrons, i.e. they exhibit limb darkening [*Eke et al.*, 2012].

[33] It should be noted that others have made different estimates of the background count rates due to neutrons outside the collimator field of view. *Lawrence et al.* [2011] found values between 1.3 and 2.25 cps, and *Eke et al.* [2012] found values between 2.0 and 2.25 cps, which compare with the value of 1.1 cps found by *Mitrofanov et al.* [2011] and used in this work. The difference is as much as a factor of two, but, as will be shown below, a factor of two difference has little effect on observed count-rate differences over small spatial scales. The works cited above, however, predict very large differences in the true LEND collimated count rates. *Lawrence et al.* [2010] found values between 0.15 and 0.18 cps, and *Eke et al.* [2012] found a most likely value of ~0.05 cps. These values are much lower than the value of 1.7 cps that we use here. We shall show in section 6 that their low estimates for the true collimator counting rates are inconsistent with the LEND observations.

[34] In order to determine the spatial variation in the background, we need to know the spatial distribution of epithermal neutrons over the entire polar region since they will all contribute to the background. We make a very good first-approximation epithermal-neutron count-rate map simply by subtracting 3.3 cps—the sum of the three different background components—from the smoothed count-rate maps as shown in Figure 7.Then for every HEALPix bin we assume the spacecraft is located 50 km above the surface at that point, and we use the first-approximation maps to calculate the flux of epithermal neutrons at the spacecraft from every HEALPix bin within view of the spacecraft. The calculations take into account both the distance from the spacecraft and the neutron flux as a function of emission angle. This flux is normalized to 0.8 cps to account for the lunar neutrons scattered off the spacecraft. To get the flux of lunar neutrons that are transmitted through the walls of the collimator, we calculate the flux in the same way, except that we also attenuate the flux as function of the angle from the collimator boresight using the angular dependence measured in the laboratory. We normalize this result to 0.3 cps, and these two background calculations then are summed together with the position-independent 2.2 cps due to cosmic-ray interactions with the spacecraft. The results are position-dependent background maps for each polar region, shown for the south in Figure 9. These background maps are then subtracted from the weighted mean maps to generate the final background corrected count-rate maps.

[35] The south polar background map shows a shallow and broad minimum that looks somewhat like a map of epithermal neutrons made with the omni-directional sensors on LEND [*Litvak et al.*, 2012a] or LPNS [*Feldman et al.*, 1998a]. This result is to be expected, of course, because the background neutrons depend on the neutron emission within the entire view of the spacecraft, which is exactly what omni-directional sensors see. The dynamic range in the background map is less than that observed by the uncollimated sensors, however, because two-thirds of the signal is the position-independent flux due to cosmic rays, and the neutrons leaking through the walls of the collimator are very well attenuated at entrance angles less than 30°. The near-nadir flux, to which uncollimated sensors are the most sensitive, is therefore not a significant contribution to the background.

[36] It was mentioned above that estimates of the background contributions could be uncertain on the order of ±0.2 cps, but it is important to recognize that regardless of the average value of the background count rate, variations in count rate over the small spatial scales of the LEND collimator field of view are insignificant. The half-area of the collimator FOV is 5 km in radius, which is small compared to that of the area that contributes to the background, which is greater than 400 km in radius. A small displacement of the spacecraft, *e.g.* 20 km, will completely change the surface seen by the collimator FOV, but will have only a small change in the very large surface area contributing to the background count rate. It can be seen from Figure 9 that the background count rate changes by only 0.017 cps over the entire region within 8° of the South Pole. If we were to use the factor of two higher values for background due to lunar neutrons suggested by *Lawrence et al.* [2010] and *Eke et al.* [2012], the background variations would still be a small 0.034 cps over the entire polar region. Over the small spatial scale of the NSRs, the background variation is much smaller still.

5. Defining the NSRs

[37] In order to determine the extent of flux suppression associated with the NSRs, we have to define the reference

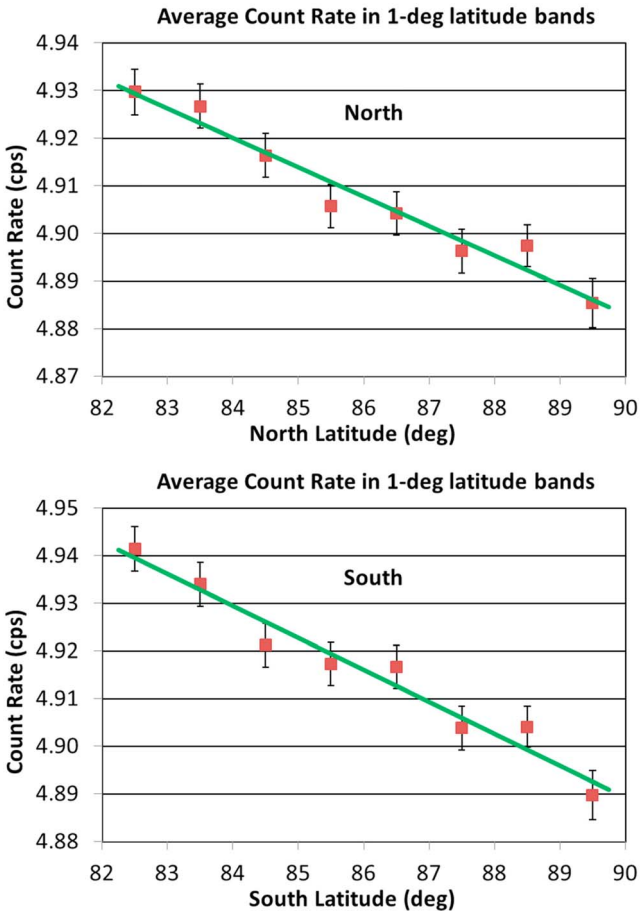

Figure 10. Count rates as a function of latitude in one-degree bands. The linear fit to these data as a function of latitude are used as the reference count rates for the count-rate difference maps. The error bars are standard errors.

level from which we calculate the suppression. We found that independent of the NSRs, the average epithermal-neutron count rate decreases with increasing latitude, and we therefore calculate the suppression relative to this latitude-dependent neutron flux. We first determine the average count rates as a function of latitude in one-degree latitude bands from the background-corrected, unsmoothed count-rate map; at this point we do not exclude any NSRs, as they are not yet defined. The count rates in the different latitude bands are similar to those shown in Figure 10. We fit the latitude-dependent count rates to a straight line and generate a difference map by subtracting the value of the line at the appropriate latitude from the background-corrected map. We then smooth this difference map, determine which HEALPix bins have count-rate differences of less than −0.04 cps, and recalculate the latitude averages excluding those bins. These new latitude averages are used to generate a new line that is used to generate the final difference map. The final smoothed difference maps are shown in Figure 11.

[38] The count rate difference used to define the NSRs is subjective. We define an NSR as a region that has a count-rate difference that exceeds −0.04 cps and has at least one location where the difference exceeds −0.06 cps. In addition, in order to eliminate small NSRs that could be just noise, we did not consider any NSRs that are smaller than 78 km^2, which is the area of the half-maximum field of view. The resultant NSRs are shown in Figure 11.

[39] Figure 12 shows the uncertainties in this map expressed in units of count rate difference relative to the standard error of the mean. It can be seen that the NSRs are all significant at the 3-sigma level or greater. It is worth noting that the flux suppressions shown in Figure 11 are relative to local material of the same latitude which already shows significant flux suppression relative to lower latitudes.

6. Data Quality

[40] Because the NSRs show only small differences in count rates from their surroundings, it is important to demonstrate the high quality of the data from the LEND collimated sensors. In this section we will demonstrate three aspects of the data that are relevant to determining their quality: 1. showing that counting statistics correctly account for all sources of random error, 2. showing that the instrument has high spatial resolution, and 3. showing that our estimate of the true counting rate of epithermal neutrons in the collimated sensors is supported by the data.

6.1. Counting Statistics

[41] We have made the assumption that the precision of the data is determined by counting statistics, but we are aware that often there are other sources of random error that may not be known. In order to confirm that our estimates of statistical uncertainty are correct, we can quantitatively test for other sources of random error that are not properly accounted for. In the polar regions the spacing between orbit tracks is small enough that many different records are averaged together to generate the weighted-mean count rate in each HEALPix bin (see section 3). As noted, each record is weighted according to its counting statistics, thus we can calculate a reduced chi square value for each bin according to

$$\chi^2_\delta = \frac{\Sigma\left\{(x_i - x)^2/\delta^2\right\}}{(n-1)} \tag{11}$$

where $(n - 1)$ is the number of degrees of freedom, υ, and the summation is over the number of records averaged in the bin. If the dispersion in the data is comparable to that expected based on counting statistics, the value of χ^2_δ should be approximately unity. The probability of getting values different from unity depends on n, the number of records that are averaged; larger values of n make it less likely to get values far from unity.

[42] The large number of records in the LEND data are ideal for testing the χ^2_δ validity of our counting statistics assumption. Within 82° of the South Pole, we have 60900 bins with a wide range in the number of records accumulated in each bin; bins closer to the poles have more records contributing to the weighted mean. For this test we chose the 3263 bins that each had 15 records accumulated – chosen because there are more bins with 15 records than with any other number of records. We made a histogram of the reduced chi square values for each of these bins and

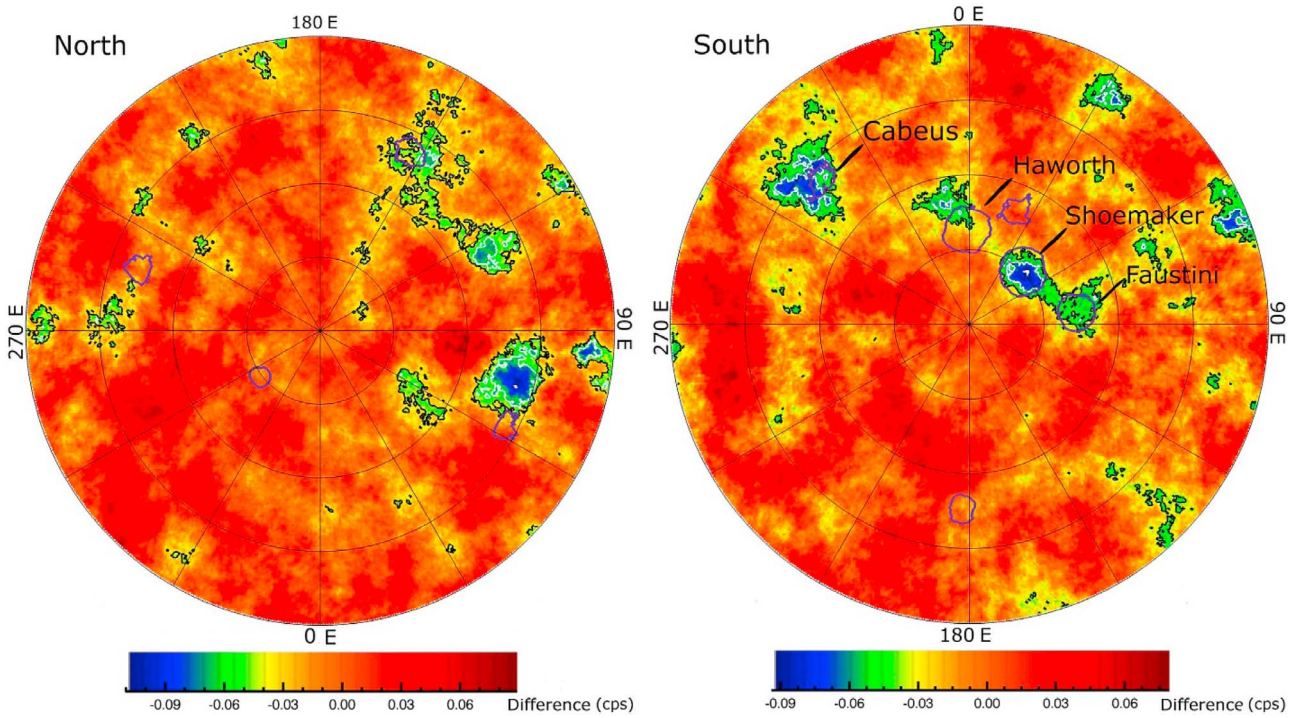

Figure 11. Count rate differences in the North and South Polar Regions to latitude 82°. The maps are made by subtracting the background (Figure 9) and taking differences from the local count rates at the same latitude (Figure 10). NSRs are regions with count-rate differences of $< -.04$ cps (black contour) that also have at least one location < -0.06 cps (white contour). The larger PSRs are shown in red outlines. It can be seen that some NSRs are associated with PSRs (Shoemaker and Cabeus), but many are not.

compared that with the expected distribution of χ^2_υ with $\upsilon = 14$ (Figure 13). It is evident from the figure that the observed probability of obtaining any particular value of reduced chi square is completely consistent with that expected based on counting statistics, indicating that there are no significant additional sources of random error in the LEND data. This analysis says nothing about systematic errors such as the exact value of the background. The systematic errors, however, will have no effect on the count-rate variations we see on the small spatial scale of the LEND collimated data, and it is this variation on small spatial scales that determine the magnitude and location of the NSRs.

6.2. Spatial Resolution

[43] Rigorously demonstrating the spatial resolution of an instrument in flight is difficult without some *a priori* knowledge of a location with high contrast. Though there are several PSRs that do not show any association with NSRs, there is one NSR near the South Pole that shows a close relationship to the Shoemaker Crater. In Figure 14 we show the Lunar Orbiter Laser Altimeter elevation profile (http://geo.pds.nasa.gov/missions/lro/lola.htm) of the crater and a trace of LEND collimator count rates along 45°E longitude, which goes through the center of the crater and continues over the pole along 225°E longitude. It can be seen that the local minimum in the count rates corresponds well to the elevation profile of the crater, suggesting that the spatial resolution of these data are adequate for finding hydrogen concentrations of size comparable to that of the Shoemaker crater.

[44] As noted in section 3, smoothing degrades spatial resolution. In Table 4 we have shown an example of the trade between spatial resolution and statistics with variable smoothing circles at the Shoemaker crater. It can be seen that as the circles get smaller, the suppression increases, due to better resolution, but the standard error gets larger. Because of the smoothing, the data in Figure 14 show a spatial resolution degraded from the true spatial resolution of LEND. The smoothing also underestimates the true extent of the neutron suppression. As an alternate way to show the effects of smoothing, we made a weighted Gaussian fit to unsmoothed data near the crater and found a suppression of -0.25 ± 0.04 cps, compared to the smoothed value of -0.18 cps. In addition, the Gaussian fit had a width equivalent to a half-area signal of 5.4 ± 1.4 km, which agrees with the pre-launch estimate of 5 km [*Mitrofanov et al.*, 2008].

6.3. True Collimator Counting Rate

[45] Finally, in order to demonstrate that our estimate of 1.7 cps for the true epithermal-neutron counting rate of the LEND collimated sensors is supported by observations, we compare the LEND collimated count rates with those of the epithermal neutron sensors of LPNS. In order to make a comparison between instruments with different sensitivities to epithermal neutrons and with different orbital altitudes, the suppression in count rates from both instruments has

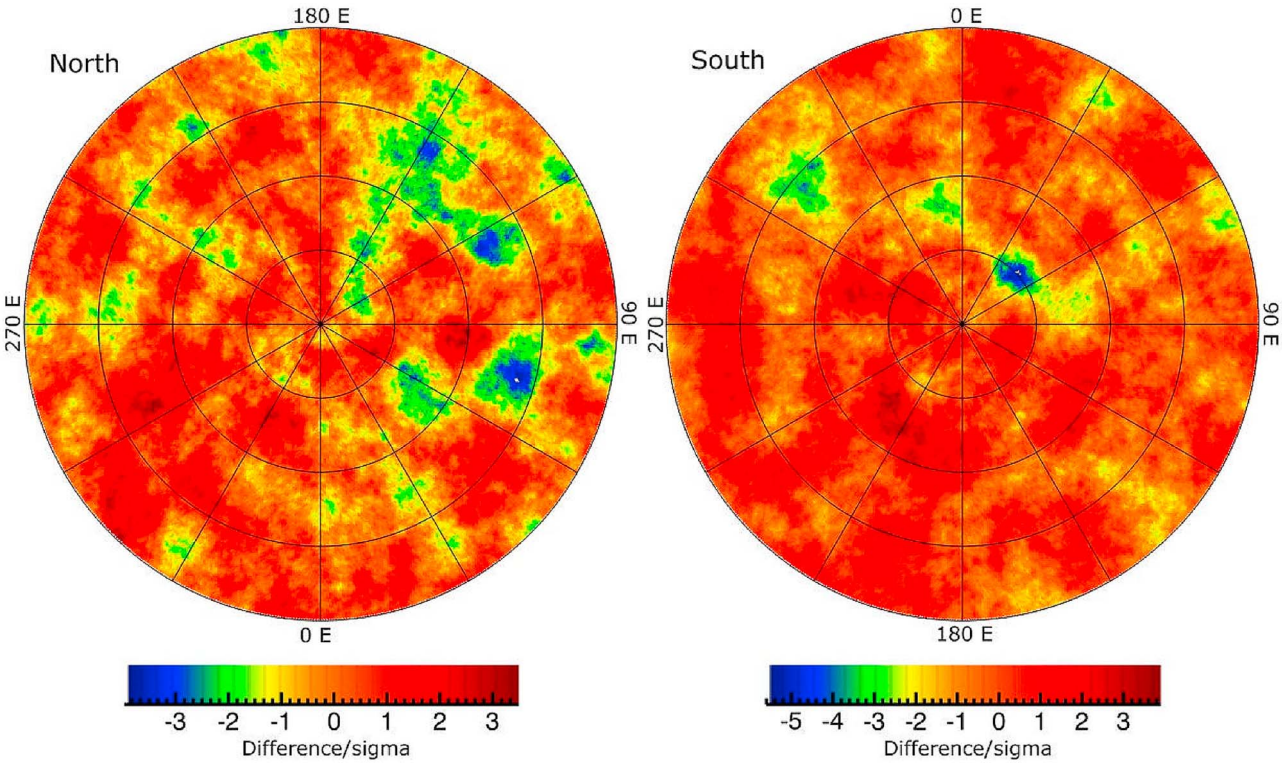

Figure 12. Uncertainties on the difference maps in Figure 11. The scale bar is in units of count-rate difference relative to count-rate standard error of the mean. Note that in both maps the NSRs are significant at the 3-sigma level or better.

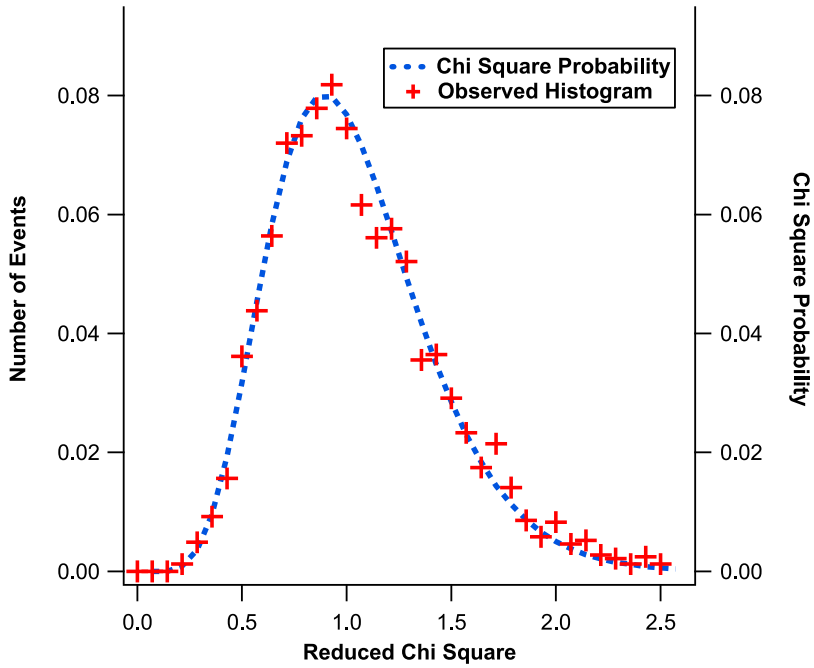

Figure 13. Histogram of reduced chi square, χ^2_δ, values for all (3263) HEALPix bins where 15 values were averaged ($\upsilon = 14$). The observed histogram is normalized to a total area of unity. The dotted line is the χ^2_δ probability distribution for a random sampling of χ^2_δ compared with the probability of returning that value from a random distribution [*Bevington and Robinson*, 1992]. Note that the dotted line is **not** a fit to the observed histogram; it is a completely independent calculation of the distribution of χ^2_δ expected for a statistically valid population with $\upsilon = 14$. It can be seen that the observed distribution agrees very well with that expected showing that counting statistics are the only significant source of random error.

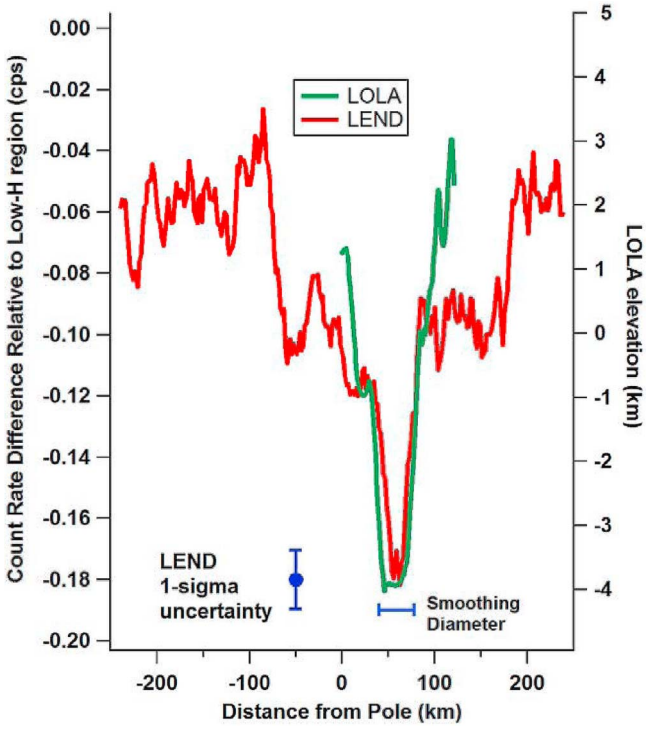

Figure 14. Background corrected epithermal-neutron count rates in the LEND collimated sensors, relative to a low-hydrogen region at lower latitudes, show spatial resolution comparable to the size of Shoemaker Crater. The LEND data are taken along the lines at 45° longitude through Shoemaker and 225° longitude on the opposite side of the pole. The smoothing that was used to decrease statistical noise decreases the magnitude of the suppression and increases its width relative to the true values. A weighted Gaussian fit to unsmoothed data near the crater shows a suppression of -0.25 ± 0.04 cps and a width of 5.4 ± 1.4 km. If leakage of neutrons through the collimator were dominating the signal as suggested by *Lawrence et al.* [2010] and *Eke et al.* [2012], the high spatial resolution observed here would not have been possible.

been converted from counts per second to relative epithermal-neutron suppression. This relative suppression is independent of sensitivity and depends only on the epithermal-neutron flux. It is defined as:

$$S = \frac{R - R_{ref}}{R_{ref}}. \quad (12)$$

where R_{ref} is a reference (unsuppressed) count rate from a region of presumed low hydrogen content and R is the count rate at the locations of interest. For this work we took the average count rate in the area bounded by 210° and 225°E longitude and by −15° and 30° N latitude as the reference count rate for the two instruments. Taking the LEND background (section 4) into account, the background-corrected count rate in this region is simply the 1.7 cps estimated by *Mitrofanov et al.* [2010a], and this value was used for R_{ref} for LEND. This background-corrected count rate is, by definition, the true collimated epithermal neutron count rate.

[46] The comparison is shown in Figure 15. The figure shows similar relative suppressions of epithermal neutrons between the two instruments indicating that the suppression of the LEND collimated sensors and LPNS is essentially identical. As noted in section 4, our estimate of 1.7 cps for the true collimated epithermal-neutron count rate is uncertain by about 0.2 cps.

[47] As noted in section 4, there have been several publications that made very different estimates of the contribution of lunar background and had very different estimates of the true LEND collimated epithermal-neutron count rate that need to be addressed. *Lawrence et al.* [2010] suggest that the reference count rate of epithermal neutrons in the LEND collimator field of view is in the range of 0.15 to 0.18 cps, which is an order of magnitude less than the value of 1.7 cps used in this work to generate Figure 15. *Eke et al.* [2012] suggested that the most likely value of this reference count rate is ∼0.05 cps. . From inspection of equation (12), it is clear that if R_{ref} were a factor of 10 smaller than the value used, the calculated relative suppressions would be a factor of 10 larger. Using values of R_{ref} that are a factor of ten smaller than 1.7 cps used here would completely negate the agreement in the values of LEND and LPNS for relative suppression. Using values for R_{ref} in the range of 0.15 to 0.18 cps as suggested by *Lawrence et al.* [2010] would yield relative suppressions on the order of 100% or more, which is completely unreasonable. Using the most likely value of ∼0.05 cps suggested by *Eke et al.* [2012] for R_{ref} is even more unreasonable.

[48] This very low value of R_{ref} prompted *Eke et al.* [2012] to suggest that the spatial resolution of LEND at 50 km altitude should be very similar to that of LPNS at 30 km altitude. Inspection of Figure 15 shows that LEND has much better spatial resolution than LPNS.

7. Discussion

[49] The H enrichment in the NSRs and the increase in H with latitude independent of the NSRs, argue for two different mechanisms for emplacement of H in the polar regions. The majority of the polar area has a systematic decrease in epithermal-neutron flux and thus an increase in

Table 4. Epithermal-Neutron Suppression in Different Size Smoothing Circles at Shoemaker Crater[a]

Radius (deg)	Suppression (cps)	Standard Deviation (cps)	Standard Error (cps)	Reduced Chisq
0.250	0.212	0.321	0.043	0.882
0.450	0.197	0.313	0.024	0.861
0.634	0.190	0.338	0.017	0.977

[a]As expected, the larger the circle, the smaller is the suppression, but the larger is the uncertainty. The reduced chi squared values near unity show that our statistical treatment of the data is valid.

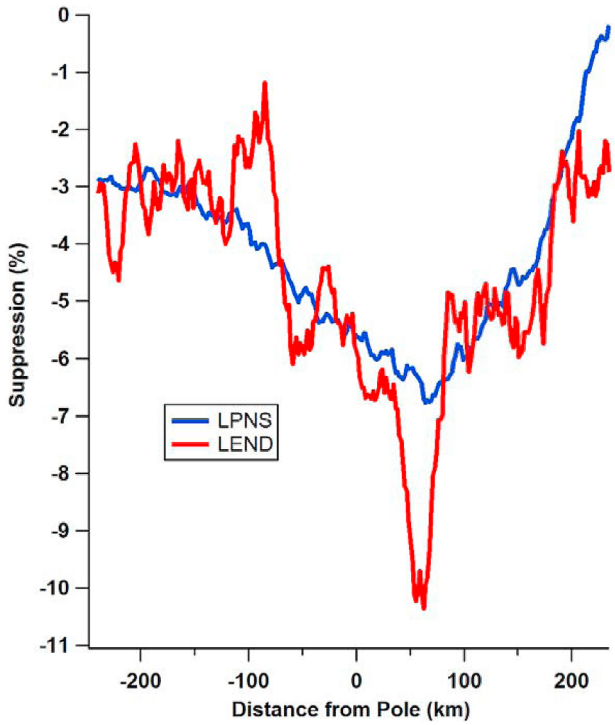

Figure 15. The LEND data from Figure 14 are compared to LPNS data and show that the spatial resolution of LEND is far better than that of LPNS, contrary to the claim of *Eke et al.* [2012]. The LPNS data were smoothed with a 15-km radius to ensure that its low spatial resolution could be seen as an intrinsic characteristic of the instrument, and that it was not due to over smoothing. The LEND data in Figure 14 were converted to relative suppression simply by dividing by our estimated collimated FOV count rate of 1.7 cps. The fact that the LEND and LPNS suppressions are comparable shows that our estimated value for the FOV count rate is accurate. If the FOV count rate were as low as that suggested by *Lawrence et al.* [2010] or *Eke et al.* [2012], the suppressions would be an impossible 100% or more.

hydrogen content toward the poles (Figure 10), and the remainder of the area has the still greater enhancement of hydrogen associated with the NSRs (Figure 11). If the latter were directly related to the PSRs, we could conclude that the greater enrichment of hydrogen in the NSRs is due to the presence of cold traps. Clearly such a direct relationship is not the case. The mechanism responsible for the concentration of hydrogen in the NSRs is not clear, nor is it the subject of this work; it is discussed in a companion paper by *Mitrofanov et al.* [2012a]. Here we will focus on this regular enhancement of hydrogen toward higher latitudes that is independent of the NSRs.

7.1. Models of Hydrogen Migration in the Lunar Polar Regions

[50] There are two obvious sources of hydrogen found on the moon: H_2O from impacts of volatile-rich comets or meteorites, and H from the sun associated with the solar wind or solar particle events (SPEs), though other sources such as lunar volcanism may contribute as well. The fate of solar-wind hydrogen on the lunar surface has been considered in great detail by *Crider and Vondrak* [2002, 2003]. They allowed for physical sputtering, chemical sputtering, and thermal desorbing. Considering all the possible mechanisms for loss and migration, *Crider and Vondrak* [2002] showed that the time it takes for the solar wind to supply the amount of hydrogen in the polar regions inferred from the LPNS data is only 7 My if all species of hydrogen are retained in the cold traps, and 100 My if only H_2O was retained. *Crider and Vondrak* [2003] performed a more thorough Monte Carlo model in which they considered the effect of volatile-poor impacts on the distribution of hydrogen. They considered both the effects of small (<1 g) impactors, which garden the soil, and larger impactors, which can bury nearby regolith with ejecta. Burial by impact would isolate water from the solar-wind loss mechanisms and preserve it until possibly being lost due to later impacts.

[51] *Schorghofer and Taylor* [2007] considered a different approach for burying surface emplaced hydrogen. They considered migration of H_2O sublimated from surface ice to grains at depth via diffusion through pore spaces, but they indicated that the long-term stability of surface ice was not likely. The surface ice would only be present following a large comet impact delivering a large volume of water to the surface. They also postulated a mechanism of thermal pumping, whereby the diurnal temperature variations allowed water vapor to migrate from warmer grains near the surface to colder grains below. When the surface is colder than the soil at depth, the migration reverses, but the rate of diffusion is much lower since the temperatures are lower. This mechanism does not require an ice phase and will slowly move water to depths deep enough to prevent loss by gardening. They concluded, however, that even subsurface ice would not survive for long periods without a surface ice layer covering it.

[52] *Siegler et al.* [2011] considered similar temperature-driven migration. They noted that under current conditions the temperatures in most shadowed areas in the polar regions are too cold for thermal migration to occur at a reasonable rate. They also noted that in the distant past the Moon had a much higher obliquity that could permit the burial of ice in places that are now too cold to support thermal migration. They defined ice traps, as distinct from cold traps, that are warm enough for water to migrate but cool enough that ice can be retained. In their model, sub-surface ice can survive for over 10^9 years in some locations, but it needs to be emplaced in an earlier time when higher obliquity allowed diffusion of water vapor.

[53] These works and many others have shown that surface ice is not permanently stable anywhere on the Moon, but it can survive for various periods of time depending on the location and burial depth. In Cabeus, one of the most hydrogen-rich areas in the south polar region (Figure 11), the LEND data imply only about 500 ppm of hydrogen assuming uniform distribution with depth [*Mitrofanov et al.*, 2010a]. We expect that the data reflect a more concentrated deposit of hydrogen that is buried beneath an H-poor surface layer. Indeed, the 5% H_2O found by LCROSS [*Colaprete et al.*, 2010] can only be reconciled with LEND data if it is buried under a significant depth of H-poor regolith.

7.2. Sources of Hydrogen Delivered to the Moon

[54] We now consider the likely sources of hydrogen on the lunar surface. The solar wind typically has a density of about 5 particles/cm^3 and a velocity on the order of 400 km/s, yielding a flux of roughly 2×10^8 particles/cm^2/s, but this value varies widely over short time periods. *Arnold* [1979] considered water brought in by impacts to be roughly 5×10^3 kg/y from small bodies (<1 g), and up to a factor of ten greater than that for larger bodies including comets. If we convert the solar-wind hydrogen flux to the equivalent amount of water delivered to the moon, we find it is about 6×10^6 kg/y, which greatly exceeds the time average that is brought in by impacts.

[55] As noted above, *Crider and Vondrak* [2003] studied in detail the fate of solar wind deposited hydrogen. They found that 12% of the solar wind hydrogen was delivered to cold traps in the polar regions. Most of the transport is in the form of OH, but as one might expect, depending on the various mechanisms for sputtering, desorption, and transport, the chemical form of the H can change many times.

7.3. Accounting for the Observed Increase in Hydrogen With Increasing Latitude

[56] We will now consider the increase in non-NSR hydrogen with increasing latitude (Figure 10) to examine the implications for hydrogen migration. The thermal-driven models of *Schorghofer and Taylor* [2007] and *Siegler et al.* [2011] are an attempt to account for special enhancements of water associated with cold traps or ice traps. Both studies note that there is a relatively narrow temperature range where subsurface ice is long lived and that water vapor diffusion is sufficiently rapid. These models, which deal with diffusion into the regolith, are most effective over a narrow temperature range, thus it is not likely that they alone can explain the regular increase in hydrogen observed with the LEND data.

[57] On the other hand, both the solar wind fluence and solar illumination decrease with roughly the cosine of the latitude. It is immediately clear, then, that the increase in hydrogen we see cannot be related to the initial deposition by the solar wind, since the deposition would show a decrease in hydrogen toward the pole rather than an increase as observed. Impacts are the other dominant means of delivering H to the Moon, and they are expected to have a nearly isotropic distribution, so they cannot be the source of the polar enrichment. Impacts of asteroidal bodies would be favored from the ecliptic, but since the H brought in by these bodies is largely vaporized, it would follow ballistic trajectories that should be close to uniform over the globe [*Butler*, 1997]. Thus it seems clear that the enhanced H in the polar regions cannot be a primary result of the delivery mechanism. Although at the time it was not known how much H was located in the PSRs and how much was in the surrounding area, *Starukhina* [2006] analyzed different possible mechanisms to account for the polar enrichment of H found by LPNS, and also concluded that loss mechanisms, rather than the primary implantation processes, dominated the distribution of H.

[58] We will now examine whether differences between steady-state gain and loss mechanisms can account for the increase in polar H. The H implanted by the solar wind, as well as H_2O deposited from impact sources, can be mobilized by a variety of processes. *Crider and Vondrak* [2002] considered sputtering and thermal desorption from interactions with solar wind ions and solar UV flux, both of which are line-of-sight energy sources from the Sun. There are also non-line-of-sight energy sources that can dislodge H in its various forms. Particles from energetic solar particle events are nearly isotropic at the Moon, but their fluence is many orders of magnitude less than that of the solar wind. In addition, UV photons from stellar sources will contribute to H migration, but again their flux is much less than that of the Sun. *Farrell et al.* [2010] showed that an ambipolar potential on the leeward side of obstructions like mountains and crater walls can deflect some fraction of the solar wind onto the shadowed surfaces. This deflection is another potential non-line-of-sight source of energy, but since we are looking at processes acting over entire latitude bands, we will neglect this effect. *Starukhina* [2006] noted that the Earth's magnetotail could be the largest source of implanted H in the PSRs. The solar wind can, of course, both dislodge H as well as supply it to the lunar soil. If it is more effective at dislodging H, the greater abundance of the solar wind at lower latitudes can yield the lower H content observed in such regions.

[59] Before we model the migration of H, we must first convert the count-rate data into concentrations of H (in all species). To do this we calculate an epithermal-neutron suppression value as we did in section 6, except a larger reference area was chosen to provide better statistics. Following a procedure like that used by *Mitrofanov et al.* [2010a] for the Cabeus region, we take an area between 150° and 220°E. longitude and −30° and +60°N. latitude for which we find an average background-adjusted count rate of 1.6938 ± 0.0012 cps. We then take the average H content in Apollo 16 soils of 45 ppm from *Bustin et al.* [1984] as our best estimate of [H] in this area. Using this value of 45 ppm H and Figure S-1 in the supplementary online material of *Mitrofanov et al.* [2010a], we calculate a reference count rate of 1.79 cps for an H-free surface, and from the count-rate averages at the two poles, we calculate the implied H content (Table 5). The conversion of count rates to H content is obviously a function of the assumed H content in the low latitude area. If we assume the H content is only 19 ppm, the lowest found by *Bustin et al.* [1984], the implied H content in each latitude band decreases uniformly by about 16% from the 45 ppm case; and for the highest H content reported by *Bustin et al.* [1984], 76 ppm (not shown), the implied H content in the polar region increases uniformly by about 8%. Thus the ratio of H content in the latitude bands is reasonably well known even if the absolute value is more uncertain.

[60] We attempted to find a simple model whereby the H enrichment with increasing latitude could constrain the relative importance of line-of-sight gain and loss mechanisms to that of omnidirectional ones. Such a simple model could be represented by

$$[\mathrm{H}] = omni + los * \cos\,(\mathrm{lat}–0.8^\circ) \qquad (13)$$

where [H] = bulk concentration of H species in the soil and *omni* and *los* represent the combined gain and loss of H by the omnidirectional and the solar line-of-sight processes,

Table 5. Relative Suppression Factors as a Function of Latitude Calculated From Background-Adjusted Count Rates[a] (cps)

		Low Latitude Soil = 45 ppm		Low Latitude Soil = 20 ppm	
Latitude	Bkg. Adj. Count Rate	Suppression	Concentration (ppm)	Suppression	Concentration (ppm)
82.5	1.634	5.5%	120	4.5%	100
86.0	1.611	6.8%	145	5.8%	120
89.5	1.590	8.0%	200	7.1%	170

[a]Hydrogen concentration is calculated assuming two different concentrations in low-latitude soils.

respectively. The latitude was adjusted by 0.8° to account for the 1.6° orientation of the lunar spin axis to the ecliptic. We found that there was no solution to this simple equation that would account for both the low latitude H content and the slope of the high-latitude data in Table 5.

[61] Figure 16 shows a plot of count rate vs. latitude that demonstrates just how rapidly the count rate changes poleward of 75°. It is clear that a simple model solely dependent on cosine latitude will not explain the LEND data. An additional parameter not yet considered, however, is the surface temperature. The thermal vaporization of H_2O depends exponentially on 1/T; and at some point, if temperatures are low enough, thermal vaporization can become completely negligible.

[62] We suggest that at lower latitudes, thermal vaporization of H_2O is the dominant mechanism for mobilization of H species, and that this mechanism is negligible in the polar region. In addition to thermal mobilization, there is some combination of mobilization by omnidirectional and line-of-sight processes as well as a combination of loss mechanisms by both types of processes. At this time the data are not adequate to allow a quantitative estimate of the relative importance of these other processes.

[63] While it is difficult at this stage to be quantitative, some qualitative points can be used to check on order of magnitude reasonableness of this suggestion. Diviner daytime temperatures (http://geo.pds.nasa.gov/missions/lro/diviner.htm) are on the order of 200 K near 75° latitude dropping to around 160 K near 82°, with obvious variations due to topography. *Hibbits et al.* [2011] studied the residence time of water molecules on the surface of lunar grains using temperature-programmed desorption measurements. They found residence times of 10^6 seconds at 160 K, and 100 seconds at 200 K, which are consistent with the suggestion above that the vaporization rate at the poles would be much lower than it is at low latitudes. It is instructive to at least crudely estimate the rate of volatilization from the regolith to see if a thermal loss process could reasonably dominate the loss of H from grains at low latitudes.

7.4. A Qualitative Model for Hydrogen Migration

[64] It is known that a significant fraction of H species is surface correlated in lunar soils. For example, [*DesMarais et al.*, 1974] analyzed H in size fractions of Apollo 15 and 16 soils and found an average of about 60 nmoles H/cm^2 (4×10^{16} molecules/cm^2) that was surface correlated. This

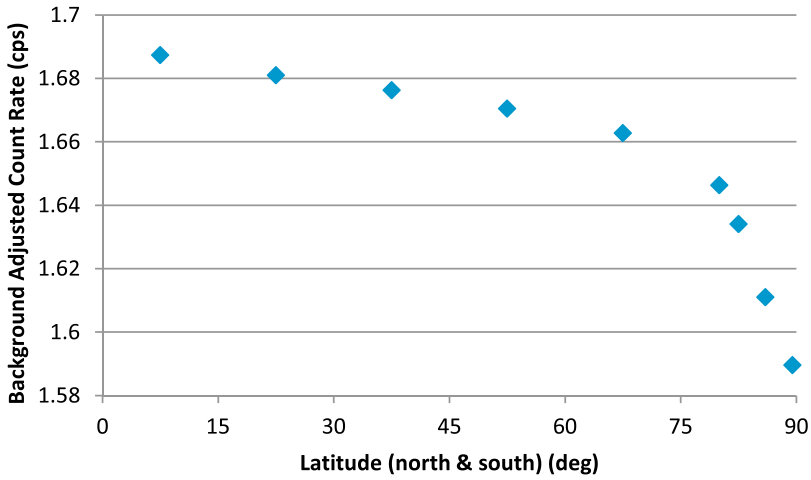

Figure 16. Average epithermal-neutron count rate in latitude bands with north and south latitudes combined. The error bars are comparable to the size of the markers. The latitudes greater than 75° are averaged over all longitudes, but with the locations of NSRs removed; the lower latitude data are averaged over longitudes from 90° to 250°E longitudes to avoid the lunar mare which generate a higher background due to interference from a greater flux of fast neutrons there. It can be seen that the count rate drops very slowly with latitude at low latitudes but falls off rapidly at high latitudes. We suggest that the change in slope at high latitudes is due to much slower thermal mobilization at the cold temperatures in the Polar Regions.

amount is actually slightly greater than a monolayer of water molecules, but the surface-correlated lunar H is not located on the molecular-scale surface. The H is embedded to depths on the order of 1000 Å [*Leich et al.*, 1973]. (To avoid confusion, we shall refer to this region of embedded H as the rim.) The amount of H on the molecular surface will be determined by the steady-state conditions of equilibration with H in the rims and with H in the lunar exosphere.

[65] The exosphere consists of H_2O and OH molecules on ballistic trajectories that are essentially isotropic over the entire lunar surface [*Butler et al.*, 1997]. The vaporization rate, however, will vary by many orders of magnitude between the equator and the polar regions, and the molecular surface abundance will similarly vary by many orders of magnitude over latitude. Clearly at low latitudes the amount of H on the molecular surface must be trivial compared to the bulk H content of the soil.

[66] *Holmes et al.* [1973] found that an Apollo 16 soil had a BET [*Brunauer et al.*, 1938] surface area of about 0.4 m^2/g. Assuming a bulk density of 1.5 g/cm^3 for the regolith and assuming that the upper 40 μm (half of the mean grain size of an Apollo 15 soil [*Heiken et al.*, 1991]) is equilibrating with the atmosphere, we find about 20 cm^2 of BET grain surface area per cm^2 of regolith. From Table 5 we can see that the soil at 86° latitude has an excess of 100 ppm H compared with the low latitude soil. The amount of H on the molecular surface to account for the excess H is about 7×10^{15} molecules of H_2O/cm^2 of grain surface, which is nearly a monolayer of water molecules. Although this is another rough estimate, it shows that the amount of H needed on the surface to account for the observed H enrichment is reasonable.

[67] *McCord et al.* [2011], using data from the Moon Mineralogy Mapper (M^3), found an increase toward the poles in two spectroscopic features thought to be related to OH, but in their data the increase began at significantly lower latitudes, around 45°. It is hard to make a quantitative comparison of their data with these data, but what could be happening is that the increase in surface H_2O begins at lower latitudes than those where LEND can detect it; M3, being sensitive to surface OH, may be able to see the surface increase in H at lower latitudes. In addition, *Sunshine et al.* [2009] and *Pieters et al.* [2009] found evidence for enhanced concentrations of surficial water molecules that were not present in sunlit portions of the regolith, and *Sunshine et al.* [2009] showed that the amount of surficial H_2O varied with time of day at the same locations. All of these observations are consistent with the suggestion that the temperature of the grains is controlling the distribution of hydrogen on the surface and that this mobility happens on a very short time scale.

[68] This transient surface H, even in the polar regions, is not sufficiently abundant that it could be detected by LEND. The reason the enhanced H in the polar regions can be detected is that the transient surface H in the high latitudes will get gardened to depth over a long time scale. The H in the polar soils will thus still be at a steady-state concentration, but it will be at a higher concentration than at lower latitudes due to less effective volatilization.

[69] In this discussion we have ignored the effect of topography, but clearly pole-facing slopes in the polar region will be colder than equator facing slopes, and thus one would expect the pole-facing slopes to have enhanced H over equator-facing slopes. The ambipolar charging noted by *Farrell et al.* [2010] could, of course, further complicate attempts to understand the effect of topography on H concentration. The biggest topographic features are the PSRs, some of which have associated NSRs and others do not. Why this is the case is still a conundrum.

8. Summary

[70] The collimated sensors of the LEND instrument return exceptionally high quality data. The spatial resolution is substantially better than that of LPNS, and the random uncertainties in the data have no other significant source of error beyond that due to counting statistics. The polar maps made from the LEND data show several local regions with epithermal-neutron suppression having a confidence level greater than 3 sigma. These neutron suppressed regions (NSRs) are not closely related to the permanently shadowed regions near the poles.

[71] The parts of the polar regions not comprised of NSRs show a significant increase in H content with increasing latitude. There is a small dependence of H content on latitude at lower latitudes, but the change becomes much more significant at latitudes higher than about 75°. We attribute this increase to a balance between the rates of gain and loss of H with the loss being dominated by thermal vaporization at lower latitudes. Because thermal vaporization is greatly reduced at high latitudes, the amount of H on the molecular surfaces there is substantially greater than at lower latitudes. Gardening of the lunar regolith distributes this higher amount of surface H throughout the bulk of the regolith accounting for the increase in H seen in the polar regions by LEND.

Notation

BET	Brunauer, Emmett and Teller [*Brunauer et al.*, 1938]
CSETN	Collimated Sensors of Epithermal Neutrons Counts per second (cps)
DAN	Dynamic Albedo of Neutrons
FOV	Field of view
FWHM	full width at half maximum
GRS	Gamma-Ray Spectrometer
HEND	High-Energy Neutron Detector
LEND	Lunar Exploration Neutron Detector
LPNS	Lunar Prospector Neutron Spectrometer
LRO	Lunar Reconnaissance Orbiter
MSL	Mars Science Laboratory
MC	Module of Collimation
NS	Neutron Spectrometer
MSE	Module of Sensors and Electronics
M^3	Moon Mineralogy Mapper
SETN	Sensor for Epithermal Neutrons
SEP	Solar Energetic Particle

[72] **Acknowledgments.** This work is dedicated to Gerard Droege, a great friend and brilliant colleague, who recently passed away after a long fight with cancer. His intellectual contribution to this work, for which we will be forever grateful, was extraordinary. This work was supported in part by NASA grant NNX09AW01G. The McMurdo neutron monitor is

operated by the University of Delaware Bartol Research Institute with support from NSF grant ANT-0739620. We are grateful for reviews from N. Schorghofer, M. Siegler, and several anonymous reviews, all of which helped improve the work substantially.

References

Arnold, J. R. (1979), Ice in the lunar polar regions, *J. Geophys. Res.*, *84*, 5659–5668.

Bevington, P. R., and D. K. Robinson (1992), *Data Reduction and Error Analysis for the Physical Sciences*, McGraw Hill, New York.

Boynton, W. V., et al. (2002), Distribution of hydrogen in the near surface of Mars: evidence for subsurface ice deposits, *Science*, *297*, 81–85.

Boynton, W. V., et al. (2004), The Mars Odyssey Gamma-Ray Spectrometer instrument suite, *Space Sci. Rev.*, *110*, 37–83.

Brunauer, S., P. H. Emmett, and E. Teller (1938), Adsorption of gases in multimolecular layers, *J. Am. Chem. Soc.*, *60*, 309–319, doi:10.1021/ja01269a023.

Bustin, R., R. K. Kotra, E. K. Gibson, G. A. Nace, and D. S. McKay (1984), Hydrogen abundances in lunar soils, *Lunar Planet. Sci.*, *XV*, 112–113.

Butler, B. J. (1997), The migration of volatiles on the surfaces of Mercury and the Moon, *J. Geophys. Res.*, *102*, 19,283–19,291.

Colaprete, A., et al. (2010), Detection of water in the LCROSS ejecta plume, *Science*, *330*, 463–468, doi:10.1126/science.1186986.

Crider, D. H., and R. R. Vondrak (2002), Hydrogen migration to the lunar poles by solar wind bombardment of the Moon, *Adv. Space Res.*, *30*, 1869–1874.

Crider, D. H., and R. R. Vondrak (2003), Space weathering effects on lunar cold trap deposits, *J. Geophys. Res.*, *108*(E7), 5079, doi:10.1029/2002JE002030.

DesMarais, D. J., J. M. Hayes, and W. G. Meinschein (1974), The distribution in lunar soil of hydrogen released by pyrolysis, *Geochem. Cosmochim. Acta*, *2*, 1811–1822.

Drake, D. M., W. C. Feldman, and B. M. Jakosky (1988), Martian neutron leakage spectra, *J. Geophys. Res.*, *93*, 6353–6368.

Eke, V. R., L. F. A. Teodoro, D. J. Lawrence, R. C. Elphic, and W. C. Feldman (2012), A quantitative comparison of lunar orbital neutron data, *Astrophys. J.*, doi:10.1088/0004-637X/747/1/6, in press.

Elphic, R. C., V. R. Eke, L. F. A. Teodoro, D. J. Lawrence, and D. B. J. Bussey (2007), Models of the distribution and abundance of hydrogen at the lunar south pole, *Geophys. Res. Lett.*, *34*, L13204, doi:10.1029/2007GL029954.

Evans, L. G., R. D. Starr, J. Bruckner, R. C. Reedy, W. V. Boynton, J. I. Trombka, J. O. Goldsten, J. Masarik, L. R. Nittler, and T. J. McCoy (2001), Elemental composition from gamma-ray spectroscopy of the NEAR-Shoemaker spacecraft's landing site on Eros, *Meteorit. Planet. Sci.*, *36*, 1639–1660.

Farrell, W. M., T. J. Stubbs, J. S. Halekas, R. M. Killen, G. T. Delory, M. R. Collier, and R. R. Vondrak (2010), Anticipated electrical environment within permanently shadowed lunar craters, *J. Geophys. Res.*, *115*, E03004, doi:10.1029/2009JE003464.

Feldman, W. C., S. Maurice, A. B. Binder, B. L. Barraclough, R. C. Elphic, and D. J. Lawrence (1998a), Fluxes of fast and epithermal neutrons from Lunar Prospector: evidence for water ice at the lunar poles, *Science*, *281*, 1496–1500.

Feldman, W. C., B. L. Barraclough, S. Maurice, R. C. Elphic, D. J. Lawrence, D. R. Thomsen, and A. B. Binder (1998b), Major compositional units of the moon: lunar prospector thermal and fast neutrons, *Science*, *281*, 1489–1493.

Feldman, W. C., D. J. Lawrence, R. C. Elphic, B. L. Barraclough, S. Maurice, I. Genetay, and A. B. Binder (2000), Polar hydrogen deposits on the Moon, *J. Geophys. Res.*, *105*, 4175–4196.

Feldman, W. C., et al. (2004), Global distribution of near-surface hydrogen on Mars, *J. Geophys. Res.*, *109*, E09006, doi:10.1029/2003JE002160.

Goldsten, J. O., et al. (2007), The MESSENGER gamma-ray and neutron spectrometer, *Space Sci. Rev.*, *131*, 339–391.

Gorski, K. M., E. Hivon, A. J. Banday, B. D. Wandelt, F. K. Hansen, M. Reinecke, and M. Bartelmann (2005), HEALPix: A framework for high-resolution discretization and fast analysis of data distributed on a sphere, *Astrophys. J.*, *622*, 759–771.

Heiken, G., D. Vaniman, and B. M. French (Eds.) (1991), *Lunar Sourcebook: A User's Guide to the Moon*, Cambridge Univ. Press, New York.

Hibbits, C. A., G. A. Grieves, M. J. Poston, M. D. Dyar, A. B. Alexandrov, M. A. Johnson, and T. M. Orlando (2011), Thermal stability of water and hydroxyl on the surface of the Moon from temperature-programmed desorption measurements of lunar analog materials, *Icarus*, *213*, 64–72.

Holmes, H. F., E. L. Fuller, and R. B. Gammage (1973), Interaction of gases with lunar materials: Apollo 12, 14, and 16 samples, *Geochim. Cosmochim. Acta*, *3*, 2413–2423.

Knoll, G. F. (2000), *Radiation Detection and Measurement*, John Wiley, Hoboken, N. J.

Lawrence, D. J., W. C. Feldman, B. L. Barraclough, A. B. Binder, R. C. Elphic, S. Maurice, and D. R. Thomsen (1998), Global elemental maps of the Moon: The Lunar Prospector Gamma-Ray Spectrometer, *Science*, *281*, 1484–1489.

Lawrence, D. J., W. C. Feldman, R. C. Elphic, J. J. Hagerty, S. Maurice, G. W. McKinney, and T. H. Prettyman (2006), Improved modeling of Lunar Prospector neutron spectrometer data: implications for hydrogen deposits and the lunar poles, *J. Geophys. Res.*, *111*, E08001, doi:10.1029/2005JE002637.

Lawrence, D. J., R. C. Elphic, W. C. Feldman, H. O. Funsten, and T. H. Prettyman (2010), Performance of orbital neutron instruments for spatially resolved hydrogen measurements of airless planetary bodies, *Astrobiology*, *10*, 183–200.

Lawrence, D. J., E. Eke, R. C. Elphic, W. C. Feldman, H. O. Funsten, T. H. Prettyman, and F. A. Teodoro (2011), Technical comment on "Hydrogen mapping of the lunar south pole using the LRO Neutron Detector Experiment LEND," *Science*, *334*(6059), 1058.

Leich, D. A., T. A. Tombrello, and D. S. Brunett (1973), The depth distribution of hydrogen and fluorine in lunar samples, *Geochim. Cosmochim. Acta*, *2*, suppl. 4, 1597–1612.

Litvak, M. L., et al. (2008), The Dynamic Albedo of Neutrons (DAN) experiment for NASA's 2009 Mars Science Laboratory, *Astrobiology*, *8*, 605–612.

Litvak, M. L., et al. (2012a), Global maps of lunar neutron fluxes from the LEND instrument, *J. Geophys. Res.*, *117*, E00H22, doi:10.1029/2011JE003949.

Litvak, M. L., et al. (2012b), LEND neutron data processing for the mapping of the Moon, *J. Geophys. Res.*, *117*, E00H32, doi:10.1029/2011JE004035.

Maurice, S., D. J. Lawrence, W. C. Feldman, R. C. Elphic, and O. Gasnault (2004), Reduction of neutron data from Lunar Prospector, *J. Geophys. Res.*, *109*, E07S04, doi:10.1029/2003JE002208.

McCord, T. B., L. A. Taylor, J.-P. Combe, G. Kramer, C. M. Pieters, J. M. Sunshine, and R. N. Clark (2011), Sources and physical processes responsible for OH/H_2O in the lunar soil as revealed by the Moon Mineralogy Mapper (M^3), *J. Geophys. Res.*, *116*, E00G05, doi:10.1029/2010JE003711.

Metzger, A. E., J. I. Trombka, L. E. Peterson, R. C. Reedy, and J. R. Arnold (1973), Lunar surface radioactivity: Preliminary results of the Apollo 15 and Apollo 16 gamma ray spectrometer experiments, *Science*, *179*, 800–803.

Mitrofanov, I. G., et al. (2002), Maps of subsurface hydrogen from the High Energy Neutron Detector Mars Odyssey, *Science*, *297*, 78–81.

Mitrofanov, I. G., et al. (2008), Experiment LEND of the NASA Lunar Reconnaissance Orbiter for high-resolution mapping of neutron emission of the Moon, *Astrobiology*, *8*(4), 793–804.

Mitrofanov, I. G., et al. (2010a), Hydrogen mapping of the lunar south pole using the LRO Neutron Detector Experiment LEND, *Science*, *330*, 483–486.

Mitrofanov, I. G., et al. (2010b), Lunar Exploration Neutron Detector for the NASA Lunar Reconnaissance Orbiter, *Space Sci. Rev.*, *150*(1–4), 183–207.

Mitrofanov, I. G., W. V. Boynton, M. L. Litvak, A. B. Sanin, and R. D. Starr (2011), Response to comment on "Hydrogen mapping of the lunar south pole using the LRO Neutron Detector Experiment LEND," *Science*, *334*, 1058, doi:10.1126/science.1203483.

Mitrofanov, I., et al. (2012a), Testing polar spots of water-rich permafrost on the Moon: LEND observations onboard LRO, *J. Geophys. Res.*, *117*, E00H27, doi:10.1029/2011JE003956.

Mitrofanov, I. G., et al. (2012b) Dynamic Albedo of Neutrons (DAN) experiment onboard NASA's Mars Science Laboratory, *Space Science Rev.*, *170*, 559–582, doi:10.1007/s11214-012-9924-y.

Nozette, S., C. L. Lichtenberg, P. Spudis, R. Bonner, W. Ort, E. Malaret, M. Robinson, and E. M. Shoemaker (1996), The Clementine bistatic radar experiment, *Science*, *274*, 1495–1497.

Pieters, C. M., et al. (2009), Character and spatial distribution of OH/H_2O on the surface of the Moon seen by M3 on Chandrayaan-1, *Science*, *326*, 568–572, doi:10.1126/science.1178658.

Prettyman, T. H., et al. (2003), Gamma-Ray and Neutron Spectrometer for the Dawn mission to 1 Ceres and 4 Vesta, *IEEE Trans. Nuclear Sci.*, *50*(4), 1190–1197.

Schorghofer, N., and G. F. Taylor (2007), Subsurface migration of H_20 at lunar cold traps, *J. Geophys. Res.*, *122*, E02010, doi:10.1029/2006JE002779.

Siegler, M. A., B. G. Fills, and D. A. Paige (2011), Effects of orbital evolution on lunar ice stability, *J. Geophys. Res.*, *116*, E03010, doi:10.1029/2010JE003652.

Simpson, R. A., and G. L. Tyler (1999), Reanalysis of Clementine bistatic radar data from the lunar south pole, *J. Geophys. Res.*, *104*, 3845–3862.
Stacey, N., D. B. Campbell, and P. G. Ford (1997), Arecibo radar mapping of the lunar poles, *Science*, *276*, 1527–1530.
Starukhina, L. V. (2006), Polar regions of the moon as a potential repository of solar-wind-implanted gases, *Adv. Space Res.*, *37*, 50–58.
Sunshine, J. M., T. L. Farnham, L. M. Feaga, O. Groussin, F. Merlin, R. E. Milliken, and M. F. A'Hearn (2009), Temporal and spatial variability of lunar hydration as observed by the Deep Impact spacecraft, *Science*, *326*, 565–568, doi:10.1126/science.1179788.
Vinogradov, A. P., Y. A. Surkov, G. N. Chernov, F. F. Kirnozov, and G. B. Nazarkina (1966), Measurement of the gamma radiation of the lunar surface by the Luna-10 spacecraft, *Cosmic Res., Engl. Transl.*, *4*, 751–755.
Watson, K., B. Murray, and H. Brown (1961), On the possible presence of ice on the Moon, *J. Geophys. Res.*, *66*, 1598–1600.